Domain wall dynamics in two-dimensional van der Waals ferromagnets

Dina Abdul-Wahab[1], Ezio Iacocca[2,3], Richard F. L. Evans[4], Amilcar Bedoya-Pinto[5], Stuart Parkin[5], Kostya S. Novoselov[6,7] & Elton J. G. Santos[8,9†]

[1]*School of Mathematics and Physics, Queen's University Belfast, BT7 1NN, UK*

[2]*Center for Magnetism and Magnetic Materials, University of Colorado at Colorado Springs, Colorado Springs, CO 80918, USA*

[3]*Department of Mathematics, Physics, and Electrical Engineering, Northumbria University, Newcastle upon Tyne, NE1 8ST, UK*

[4]*Department of Physics, The University of York, YO10 5DD, UK*

[5]*NISE Department, Max Planck Institute of Microstructure Physics, Halle, Germany*

[6]*Department of Material Science & Engineering, National University of Singapore, Block EA, 9 Engineering Drive 1, 117575, Singapore*

[7]*Chongqing 2D Materials Institute, Liangjiang New Area, Chongqing 400714, China*

[8]*Institute for Condensed Matter Physics and Complex Systems, School of Physics and Astronomy, The University of Edinburgh, EH9 3FD, UK.*

[9]*Higgs Centre for Theoretical Physics, The University of Edinburgh, EH9 3FD, UK*

[†]*Corresponding author: esantos@ed.ac.uk*

Domain wall motion is in the core of many information technologies ranging from storage[1], processing[2], sensing[3] up to novel racetrack memory architectures[4]. The finding of magnetism

in two-dimensional (2D) van der Waals (vdW) materials[5–8] has offered a new frontier for the exploration and understanding of domain walls at the limit of few atom-thick layers. However, to use 2D vdW magnets for building spintronics nanodevices such as domain-wall based logic[9–11], it is required to gain control of their domain wall dynamics by external driving forces such as spin-polarized currents or magnetic fields which has so far been elusive. Here we show that electric currents as well as magnetic fields can efficiently move domain walls in the recently discovered 2D vdW magnets CrI_3 and $CrBr_3$ at low temperatures, and robust down to monolayer. We realize field- and current-driven domain wall motion with velocities up to 1020 m s^{-1} which are comparable to the state-of-the-art materials for domain-wall based applications[12–16]. Domain walls keep their coherence driven by the spin-transfer torque induced by the current and magnetic field up to large values of about 12×10^9 A cm^{-2} and 5 T, respectively. For larger magnitudes of current or field, a transition to a hydrodynamic spin-liquid regime is observed with the emission of a periodic train of spin-wave solitons with modulational instability[17]. The emitted waveform achieves terahertz (THz) frequency in a wide range of field and current densities which opens up perspectives for reconfigurable magnonic devices. Moreover, we found that these spin-waves can transport spin angular momentum through the layers over distances as long as 10 μm without losses for the transport of spin information. Our results push the boundary of what is currently known about the dynamics of domain walls in 2D vdW ferromagnets and unveil strategies to design ultrathin, high-speed and high-frequency spintronic devices.

Spin-based applications have been broadly explored for high-performance solid-state data storage technologies[18,19]. A promising strategy is to encode bits in magnetic domains walls which can be controlled via applied magnetic fields and spin-polarized currents[4,9]. Several approaches for domain wall-based memory devices with a focus on the domain wall displacement have been developed. From a field-controlled shift register[9,20] up to the non-volatile multi-turn sensors[21], which are commercially available[22], these emerging technologies provide a new horizon for advanced materials to be explored. With the discovery of magnetism in vdW layered compounds[5–7] and proof-of-concept devices[8,23–25] already showing outstanding progress toward applications, one of the main challenges is the integration of 2D magnets in domain wall microelectronic platforms.

Due to scaling reasons and high-density requirements[26], competitive devices should have narrow domain walls (ideally in the range of $1-10$ nm), use out-of-plane magnetic anisotropy materials and, in particular for memory devices, develop domain wall velocities of the order of $\sim$100 m s^{-1} to achieve rapid operating speed on increasing areal density[4,27]. Sufficiently low current densities ($\sim 10^6 - 10^8$ A cm^{-2}) are also needed to guarantee low power consumption and to avoid damage due to Joule heating. However, metallic layers inherently suffer with energy dissipation via the conduction electrons[2] which make magnetic insulators better suited for domain wall applications. There have been a few reports on the creation of different interfaces using magnetic vdW materials[28,29] and heavy metal overlayers (e.g. Pt, Ta) where spin-transfer torque arising from charge-to-spin current conversion can effectively switch the magnetization from one state to another. Nevertheless, it is unknown how domain walls behave intrinsically in 2D magnets as current and fields are applied directly into the systems, and how efficient such layered structures

would be in domain-wall based functional devices.

Here we demonstrate domain-wall motion in monolayer CrI_3 and $CrBr_3$ by spin polarized currents and magnetic fields in a broad range of densities ($10^7 - 10^9$ A cm^{-2}) and field ($0.001-2$ T). Both dynamics occur over hybrid domain walls with Néel-Bloch characteristics with a domain wall width of about $\sim$5.30 nm. The spin-torque induced by electric currents and magnetic fields generates a rapid rotation of the magnetization at the domain wall, hence triggering its translational motion at high velocities. We record speeds of up 1020 m s^{-1} and 100 m s^{-1} with current and field, respectively, while keeping the coherence of the wall profile through a steady motion. As the domain wall velocity approaches the maximum spin-wave group velocity, the domain wall motion start to exhibit non-linear effects with the emission of magnons at terahertz (THz) frequencies following a modulational instability behaviour. Even though no conduction electrons are present in the medium due to the insulating characteristics of CrI_3 and $CrBr_3$, spin-information can be transported over distances as long as 10 μm which sets a new paradigm for spin-wave-based technologies at the ultrathin limit.

Our starting point is the investigation of the magnetic domain structures in monolayer $CrBr_3$ and their dynamic evolution under different temperatures and magnetic fields. The domain wall structure of CrI_3 and its cooling dynamics have recently been reported using similar theoretical framework[30]. We use a large square flake of 0.4 μm $\times$ 0.4 μm to represent a system able to be measured using imagining techniques, i.e. nitrogen-vacancy scanning magnetometry[31]. We describe the interactions using the following spin Hamiltonian:

$$\mathscr{H} = -\sum_{ij} J_{ij}(\mathbf{S}_i \cdot \mathbf{S}_j) - \sum_{ij} \lambda_{ij} S_i^z S_j^z - \sum_i D_i (\mathbf{S}_i \cdot \mathbf{e}_i)^2 - \sum_{ij} K_{ij} \left(\mathbf{S}_i \cdot \mathbf{S}_j\right)^2 - \sum_i \mu_i \mathbf{S}_i \cdot \left(\mathbf{B}_i + \mathbf{B}_i^{\mathrm{dp}}\right) \quad (1)$$

where $\mathbf{S}_i$ and $\mathbf{S}_j$ are the localized magnetic moments on Cr atomic sites i and j which are coupled by pair-wise exchange interactions. J_{ij} and λ_{ij} are the isotropic and anisotropic bilinear (BL) exchanges, respectively, and D_i is the single ion magnetic anisotropy. $\mathbf{B}_i$ and $\mathbf{B}_i^{\mathrm{dp}}$ represent external and dipole magnetic field sources respectively. Eq. 1 was previously found to describe accurately the magnetic properties of several 2D magnets[30,32] including CrI_3 and $CrBr_3$. Comparisons with other spin Hamiltonians such as Kitaev, bilinear Heisenberg, Ising, and Dzyloshinskii-Moriya interactions, were undertaken in refs.[30,32] as well as in their Supplementary Information files. We take into account up to third nearest neighbors for J_{ij} and λ_{ij} in the description of $CrBr_3$ in Eq.1. All the parameters in Eq.1 are extracted using highly accurate non-collinear ab initio simulations taking into account spin-orbit coupling and Hubbard-U corrected density functional theory as described in Ref.[30,32]. We ensure that fine numerical convergence within $10^{-6} - 10^{-8}$ eV is achieved in each computed parameter. We also compared the exchange parameters used in our work with those collected from the literature[33]. In the context of the materials studied in our study (monolayer CrI_3 and $CrBr_3$), Supplementary Figure 1 clearly shows that our exchange magnitudes[32] reproduce with high accuracy the critical temperatures measured. Moreover, Eq.1 provides an accurate description of the magnon dispersion extracted from inelastic neutron scattering measurements on CrI_3[34] as shown in ref.[32]. These results provide a firm background for the modeling of the domain wall dynamics as described here.

The fourth term in Eq.1 represents the biquadratic (BQ) exchange which involves the hopping

of two or more electrons between two adjacent sites[32]. Its strength is given by the constant K_{ij}, which is the simplest and most natural form of non-Heisenberg coupling. It has recently been found that several 2D vdW magnets develop substantial BQ exchange in their magnetic properties which is critical to quantitatively describe important features such as Curie temperatures, thermal stability, magnon spectra and non-trivial topological spin textures[30,32,35,36]. The magnitude of K_{ij} for $CrBr_3$ is 0.22 meV which is smaller than the BL exchange for the first-nearest neighbours ($J_1 = 1.66$ meV) but still sizeable to be disregarded[32]. In our implementation the BQ exchange is quite general and can be applied to any pair-wise exchange interaction of arbitrary range. Each system is evolved by solving the atomistic Landau-Lifshitz-Gilbert equation with a Gilbert damping $\lambda_G = 0.1$ to ensure better computational efficiency and numerical stability of the time integration. The value of λ_G is substantially higher than that (2×10^{-3}) recently measured for a parent compound[37] (i.e. $CrCl_3$) which a similar magnitude would be expected for CrI_3 and $CrBr_3$. The large λ_G also accounts for the possibility of free-electron doping to raise the conductivity of the system due to different processes (i.e. dopants[38], electric bias[39]). Due to the inclusion of dipole-dipole interactions we explicitly include non-local damping effects in our simulations such as due to domain walls or different magnetic textures. Hence, our spin-dynamics simulations include an accurate description of the spin-interactions at the atomistic level ($2-20$ Å) in a multiscale framework at the lab scale (a few μm's).

Monolayer $CrBr_3$ is thermally equilibrated above 40 K and then linearly cooled to 0 K in a total simulated time of 4.0 ns at different magnetic fields (Figure 1 and Supplementary Movies S1-S4). The time evolution of the out-of-plane magnetization M_z is utilised to study the nucleation

of the magnetic domains as it determines the easy-axis throughout the layer. For zero-field cooling (0 mT) magnetic domains are formed for temperatures below 20 K with the free motion of the domain walls as the temperature drops (Fig. 1**a-e**). As the system reaches 0 K a continuous time evolution of the domain structures remains which results in a homogenous magnetization over the entire crystal (Supplementary Movie S1). Even though thermal fluctuations as well as their contributions to the energy of the system are inexistent at 0 K, other terms, such as dipolar fields, exchange interactions and magnetic anisotropy, are still present, further contributing to the modification of the magnetic domains. Once magnetic fields are applied to the nanosheet (Fig. 1**f-t** and Supplementary Movies S2-S4) this nucleation-type mechanism is accelerated with a rapid reversal in the sign of the magnetization M_z. Indeed, a monodomain feature is observed even in fields far below the coercivity[40] (10 mT at 5 K) for $CrBr_3$. In a scenario where defects or pinning sites are not present in monolayer $CrBr_3$, magnetic domains tend to be meta-stable with a homogeneous magnetisation throughout the surface. This is in sound agreement with recent NV-center scanning magnetometry measurements[31] on the magnetic domain evolution of $CrBr_3$ indicating that pinning effects are the dominant coercivity mechanisms.

Strikingly, the interplay between domain metastability and high magnetic anisotropy of $CrBr_3$ give additional characteristics to the domain walls (Figure 2**a-b**). We observe that as the spins vary orientation from one magnetic domain to another the wall profile assumes components of the magnetization along different in-plane directions ($M_{x,y}$) relative to the easy-axis (M_z) (Fig. 2**c-d**). In-plane magnetization M_x displays a variation larger than that for M_y which is mainly noticed at the core of the domain wall within $1-2.5$ nm. These features indicate a domain wall with

hybrid characteristics of Bloch and Néel type (Fig. 2**e-f**). We can extract the domain wall width $\sigma_{x,y,z}$ by fitting the different components of the magnetization (M_x, M_y, M_z) to standard equations of the form[41]:

$$M_j = \frac{1}{\cosh(\pi(j-j_0)/\sigma_j)}, \quad \text{with} \quad j = x, y \tag{2}$$

$$M_z = \tanh(\pi(z-z_0)/\sigma_z) \tag{3}$$

where j_0 and z_0 are the domain wall positions at in-plane and out-of-plane coordinates, respectively. The domain wall widths are within the range of $\sigma_{x,y,z} = 5.30 - 5.33$ nm. Materials with high magnetic anisotropy generally stabilise such small domain wall widths but their magnetic domains are generally stable after zero-field cooling due to long range dipole interactions. We have checked that the inclusion of dipolar fields in our simulations do not change the results.

An intriguing question raised by the hybrid features of the domain walls in $CrBr_3$ and CrI_3[30] is the effect of magnetic fields and electric currents on the motion of domain walls. It is well established that both driving forces can induce displacement of domain walls in magnetic thin films over different substrates. Nevertheless, the vdW nature of the nanosheet together with the atomic thickness (≈0.5 nm) may induce additional phenomena yet to be observed in 2D ferromagnets. Figure 3**a-d** shows that either fields or currents can efficiently displace domain walls in layered $CrBr_3$ and CrI_3 magnets. The dynamics is generally initialised with a domain wall at equilibrium position previously thermalized for several nanoseconds for full convergence of the spin orientations (Fig. 3**a**). The finite width of the nanowire assists in the formation of the domain walls pinned by the edges. For field-induced domain wall motion, wall velocities up to v =70 m s^{-1} and v =98 m s^{-1}

are recorded for $CrBr_3$ and CrI_3 (Fig. 4**a-b**), respectively. The wall moves steadily on both sheets and can be described as $v = \mu_F(B - B_o)$, where μ_F is the wall mobility and B_o is the onset field required to move the wall from structural defects or pinning[42]. The magnitudes of μ =0.0343 m s^{-1} mT^{-1} and $B_o = 23.89$ mT for $CrBr_3$ and μ =0.018 m s^{-1} mT^{-1} and $B_o = 13.33$ mT for CrI_3 indicate that domain walls move relatively slower than those in metallic ultrathin Pt/Co/Pt films[43] or thick magnetic insulator TmIG/Pt interfaces[14] but with relatively similar onset field B_o. The domain wall moves steadily on both sheets at fields below critical magnitudes (B_c) of $B_c = 1.19$ T and $B_c = 4.78$ T for $CrBr_3$ and CrI_3, respectively (Supplementary Movies S5-S6). For values beyond B_c different spin distributions start nucleating ahead of the domain-wall (Supplementary Movie S7-S8) and induce its collapse within a few hundreds of picoseconds after the motion initiated. These spin features appear from the edges of the layers and rapidly move into the bulk of the ribbon. This behaviour is analogous to that observed in Pt/Co/AlO_x ultrathin microstructures[44] and highlighted the importance of edges on the magnetic properties of 2D magnets in device integration. A preference for unreconstructed edges or dangling bonds rather than on zig-zag edges (Fig. 3**b** at 1.50 T) has been observed in the nucleation of reversed domains during the wall dynamics. The local variation of the exchange interactions at dangling-bonds with spins being less restricted to change their directions with an external field than at zig-zag edges is one of the main ingredients for this behaviour. This observation shall trigger further experimental studies of the atomic structure at the edges of the monolayer magnets via scanning probe microscopies[45,46] and their connection to the device performance.

In the case of current-driven domain wall motion, we state that such behaviour can be ac-

complished in two ways. First, by using an adjacent conducting layer as recently demonstrated for insulating $Tm_3Fe_5O_{12}$ on top of a Pt substrate[14]. Charge current will flow in the heavy metal generating spin currents that exert a spin-transfer torque (STT) on the ferromagnetic material. Second, by doping the CrX_3 (X=Br, I) magnets in order to generate significant carriers in the host[27,47]. Such strategies are well established and would provide a feasible platform to confirm our predictions. Indeed, we recorded domain wall velocities up to 530 m s^{-1} and 1020 m s^{-1} for monolayer $CrBr_3$ and CrI_3, respectively, under applied currents (Fig. 4**c-d**). These velocities are higher than those observed in a wide range of systems including skyrmions (100 m s^{-1})[13], ferromagnetic semiconductor (Ga, Mn)As (22 m s^{-1})[47], synthetic antiferromagnets (750 m s^{-1})[12], metallic layers (380 m s^{-1})[48], Pt/CoFe/MgO and Co/Ni/Co interfaces ($\sim$10 m s^{-1}, 400 m s^{-1})[16,49], and insulating oxides (400 m s^{-1})[14]. It is worthwhile highlighting that low current densities within the experimental range of 10^{-8} A cm^{-2} (insets in Fig. 4**c-d**) already resulted in domain wall speeds (i.e. 100 m s^{-1}) similarly as those achieved in established racetrack platforms with more complex materials[4]. The domain walls displace freely as a function of the current density j in a viscous flow motion (Supplementary Movies S9-S10). The high velocities predicted for $CrBr_3$ and CrI_3 are only limited by the spin-wave group velocity v_g intrinsic to the systems. By using a spin-wave theory for 2D magnetic materials[32], which includes biquadratic exchange and Dzyaloshinskii-Moriya interactions (DMI), we estimate from the magnon dispersion (Supplementary Figure 2) maximum values of v_g within the range of $584-891$ m s^{-1} for $CrBr_3$ and $1326-6400$ m s^{-1} for CrI_3 (Supplementary Figure 3). These values are close to those computed from the atomistic simulations (530 m s^{-1} and 1020 m s^{-1} for $CrBr_3$ and CrI_3, respectively) although slightly larger. This is due to the damping of

the domain wall motion by the emission of spin-waves[50] not taken into account into the model as commented in the following.

The steady displacement of the domain walls occurs up to a certain threshold (j_w) defined as the Walker breakdown[42]. For values below j_w, the wall dynamics can be well modelled by a simple 1D model[51,52] through a linear dependence of v and j:

$$v = \mu_I j \tag{4}$$

where μ_I is the current-driven domain-wall mobility which gives $\mu_I = 0.12 \times 10^{-10}$ m^3 A^{-1}s^{-1} and $\mu_I = 0.10 \times 10^{-10}$ m^3 A^{-1}s^{-1} for monolayer $CrBr_3$ and CrI_3, respectively. These values are of the same order of magnitude as those recorded on thin metallic interfaces[49] or permalloy nanowires[53] which have been studied more intensively. For values near j_w or above, the spins at the domain wall precesses inducing disruption of the wall at longer times with the nucleation of magnetic domains with a different polarisation ahead of the displacement of the domain-wall (Fig. 3**c** at 4.35×10^9 A cm^{-2}). A close look at these features (Fig. 3**d**) indicates that they may start from both edges although dangling-bonds may induce more curvature to the domain wall since a dragging on the motion is observed generating retardation relative to the zig-zag edge. We can model qualitatively the dynamics at $j > j_w$ for both $CrBr_3$ and CrI_3 via the time average velocity of the domain wall[51,52]. This suggests that the domain-wall dynamics in 2D magnets is similar as that in magnetic nanowires which allows faster integration into existing devices[27]. We also observe that as the domain wall moves spin-waves or magnons are emitted (Fig. 4**e-f**). The spin frequencies driven by the field (ω_B) and current (ω_J) are in the terahertz (THz) regime with maximum magnitudes of $\omega_B^{max} = 0.43$ THz and $\omega_J^{max} = 0.60$ THz for $CrBr_3$ and $\omega_B^{max} = 0.50$ THz

and $\omega_J^{max} = 0.66$ THz for CrI_3. These frequencies are in sound agreement with those estimate from the magnon dispersion along different points of the Brillouin zone for both halides (Supplementary Figure 3). We found that the maximum frequencies with the field are close to those at the M−point (0.47 THz for $CrBr_3$, and 0.57 THz for CrI_3), whereas with the applied current are around the K−point (0.63 THz for $CrBr_3$, and 0.64 THz for CrI_3). Indeed, the variations of ω_B and ω_J can be well fitted using:

$$\omega_B = \omega_0^B + \alpha_B B \quad (5)$$

$$\omega_J = \omega_0^J + \alpha_J j \quad (6)$$

where $\omega_0^B(B=0)$ and $\omega_0^J(j=0)$ are the onset frequencies resulting in $\omega_0^B = 0.29$ THz and $\omega_0^J = 0.31$ THz for $CrBr_3$; and $\omega_0^B = 0.25$ THz and $\omega_0^J = 0.43$ THz for CrI_3. We also notice that the magnitudes of ω_0^B and ω_0^J may also change due to the inhomogeneous spatial distribution of the emitted spin-waves (Supplementary Movie 11) even though with a similar behaviour with the field and current. The coefficient α_B differs moderately between both halides converging to 0.13 THz T^{-1} and 0.05 THz T^{-1} for $CrBr_3$ and CrI_3, respectively, with $\alpha_J \approx 0.04$ THz 10^{-9} A cm^{-2} being similar to both systems. On the field-driven spin-wave emission, the domain wall precesses with a frequency near the Larmor frequency $\omega_0 = \gamma B$, where γ is the gyromagnetic ratio, similarly as in nanowires[54]. We noticed that in both layered materials the spin wave frequencies are enclosed between odd- and even-numbered harmonics. That is, $CrBr_3$ is within $4\omega_0$ and $5\omega_0$ ($\omega_B - \omega_o^B = 4.81\omega_0$), and CrI_3 is within ω_0 and $2\omega_0$ ($\omega_B - \omega_o^B = 1.70\omega_0$). This indicates that the spin waves and their overtones can be excited with a combination of fundamental modes which gives additional flexibility for terahertz source of magnetic signal using atomically thin layers. In

addition, the emission of spin waves electrically-driven can be associated with the Doppler effect on the frequency shift[55]. As the domain wall moves the current changes the spin-waves dispersion and incidentally causes an effective flow of the magnetic medium. This is reflected by the linear dependence of ω_J on j (Fig. 4f) in agreement with the spin-transfer-torque Doppler shift. A similar approach has been successfully used to study the effect of electric signal into magnons in permalloy strips[56], $Ni_{80}Fe_{20}$ wires[57] and thin films[58].

A substantially different phenomenon is observed when the domain wall is subject to large current densities, $j > 10^{10}$ A cm^{-2}, with the appearance of spin hydrodynamic effects in $CrBr_3$ and CrI_3. The dynamics is illustrated in Figure 5**a-c** where we plot line-cuts of the M_z and M_x components of the magnetisation at width 25 nm and selected times for monolayer CrI_3. We observe that shortly after the electric pulse starting propagating into the system within 18-78 ps the M_x projection exhibits a wave propagating ahead of the domain wall. This amplitude tilts M_z into the plane and increases exponentially (Fig. 5**d**) until M_z is completely suppressed and eventually switches, nucleating a new domain wall. The first period of the wave in M_x or shock wave continues to propagate with no appreciable dissipation and new domain walls are nucleated in its wake with a certain periodicity (Fig. 5**a-c**). This nonlinear phenomenon is indicative of a modulational instability (MI) as observed in fluid dynamics[17,59]. This type of instability occurs in focusing media and describes the exponential growth of waves within a band of wavevectors until non-linear effects favour their spatial localisation into solitons. MI are ubiquitous in dispersive physical problems and have been observed in several systems such as in water waves[60], nonlinear optics [61] and Bose-Einstein condensates[62]. In magnetic materials however MI has been invoked

so far as a pathway for the nucleation of dissipative droplets in perpendicular magnetic anisotropy (PMA) ferromagnets[63], as well as the spatial localisation of high-energy magnons in PMA ferrimagnetic alloys excited with ultrafast optical pulses[64], and the disintegration of short-wavelength spin-superfluids in planar ferromagnets[65]. In contrast, we find clear evidence of spin hydrodynamic behaviour manifested the onset of MI and its nonlinear dynamics driven by electrical currents in 2D magnetic materials. We emphasize that the nonlinear effect observed here is fundamentally different from Walker breakdown and the subsequent precessional regime so far observed in bulk magnets.

We also observe that MI is visible already at 20 ps as the wavefront exhibits a transverse structure and can be more generally regarded as a spin shock wave (Fig.6**a-c**). At 200 ps, there are rich transverse features in the nanoribbon, from which we can identify a modulationally unstable region where new domains are established. These domains are bounded by the trailing domain-wall (soliton edge) and the spin shock wave. At 600 ps, the shock wave is already outside our simulation profile and the domain walls continue to propagate further (see Supplementary Movie S12 for the full sequence). The salient features of the MI dynamics can be visualized in Fig. 6**d** by a colour-plot of the M_z component line-cuts as a function of time. After an initial translation of the domain wall, there is a split of behaviours at ≈ 0.01 ns where we can define two characteristic speeds (dashed lines in Fig. 6**d**). The shock wave (SW) (Fig. 6**b**) translates with a speed of $s^+ = 5.77$ km s$^{-1} \pm$ 0.84 km s^{-1} which is in sound agreement with the maximum group velocity calculated for CrI_3 (Supplementary Figure 3). The soliton edge exhibits a phase-shift and subsequent translation with a speed of $s_1^- = 1.33$ km s$^{-1} \pm 0.002$ km s^{-1} (Fig. 6**b**). Consequently, the wavelength L of the

nucleated domains can be extracted from the spectral function at a constant speed, such at s^+ (Fig. 6**e**). The obtained frequency of the wavefront or SW is computed as ν_{SW} =177.5 GHz±1.25 GHz. We can immediately extract L through a simple speed and frequency relationship via $L = s^+/\nu_{SW}$ = 5.77 km s^{-1}/177.5 GHz= 32.50 ± 0.23 nm which is equivalent to a wave-vector of $k_{SW} = 2\pi/L = 0.19$ nm^{-1}±0.00003 nm^{-1}. Indeed, the shock-wave speed corresponds to the group velocity of the most unstable magnon with a wave-vector given by k_{SW}.

The growing region bounded by the speeds s^+ and s_1^- is reminiscent to the development of dispersive shock waves (DSWs)[17] which is located at the modulationally unstable region highlighted on Fig.6**b**. DSWs are ordered structures that smoothly connect the wavevectors at the front and soliton edges, and have been fully characterised for planar ferromagnets[66]. However, the MI in our system induces periodic domain-wall nucleation defined by the most unstable wavevector. Therefore, we can regard the scenario of Figs.6**b-c** as an unstable generalization of a DSW. The periodicity of the nucleated domains leads to initially similar domain-wall speeds (parallel features in the wake of the wavefront) that are later perturbed by interactions, annihilation, and nucleation events. These can be potentially related to turbulence, thermodynamic behaviour as a soliton gas[67], or rare events such as rogue waves[60]. At a later time ($\approx$ 0.04 ns), a second characteristic domain-wall speed $s_2^- = 0.88$ km s$^{-1} \pm 0.001$ km s^{-1} is observed. This second speed appears to be related to an additional source of MI in the wake of the soliton-edge that opposes the current-driven torque. We can extract the frequency of this domain-wall wake (Fig.6**f**) resulting in ν_{wake} =6.66±1.66 GHz. Given the value of s_2^-, we can extract a wavelength of 132.28±32 nm which corresponds to the periodicity of where new domain wall appears into the system induced

by the wake of the domain-wall motion.

Interestingly, we also found that in principle there is no spatial limit for the propagation of the shock waves in the systems. Simulations undertaken at a mesoscopic level (Supplementary Figure 4) showed that once an electrical excitations is applied into the system, the transmission of short-wavelength spin waves can extend for long-distances with minor disturbance from the medium. We record lengths up to 10 μm with a group velocity above $\sim$2000 m s^{-1} where spin-waves can work as nanoscale information carriers. The spatial distance is at the same order of magnitude as those previously obtained in the magnetic insulator yttrium iron garnet (YIG)[68], and ferromagnetic nanowires grown on thick YIG thin-film[69], with both have been proposed as platforms to controllable transmission of spin information. The combination between small damping ($\approx 2 \times 10^{-3}$) in this class of 2D ferromagnets[37], the insulating nature of CrI_3 and $CrBr_3$ with no conduction electrons available to induce decay in the spin signal[70] and the relative low magnon scattering[71] make magnetic layered materials a new endeavour for magnonics applications.

Discussion

The possibility to manipulate and control domain walls precisely on 2D vdW CrX_3 (X=Br, I) magnets opens up a pathway to design a range of novel and highly competitive applications in the thickness of a few atoms. As some of the critical parameters to domain-wall based devices are domain wall widths, which control the information density, domain wall motion, directly governing access time, and pinning processes, that determine the energy consumption, 2D magnets

show features that are fundamental for integration in novel memory technologies, such as racetrack memories[4]. The large domain wall speeds achieved in both $CrBr_3$ and CrI_3 at the limit of 1020 m s^{-1} compete side-by-side with the best materials used for racetrack applications (e.g. synthetic antiferromagnets[12]) where complex interfaces need to be fabricated to induce fast domain wall shifting. This remarkable result, along with recent advances in the scalable bottom-up growth of CrX_3 in the monolayer regime[72,73], clearly presents as an opportunity for reduction on manufacturing and time-consuming device preparation. There is a still a challenge that needs to be overcome to enable current-driven excitations in these 2D magnetic halides, for instance, the enhancement of the conductivity and the consequent reduction of the current densities used to move domain walls. One route is to use doping, which is a well-known strategy that has been widely employed in other prototypical ferromagnetic semiconductors (such as (Ga,Mn)As)[47]. In fact, carrier doping has been found to induce half-metallicity and enhance the ferromagnetic stability in CrI_3 monolayer[39,74], such that current-induced phenomena become feasible without compromising the magnetic properties. It is worth mentioning that some trade-off between conductivity enhancement and dissipation through the conduction electrons would have to be achieved for low-power consumption. It is well known that large Gilbert damping λ_G allows fast relaxation of the magnetization to equilibrium, whereas low damping enables energy-efficient processes. Several approaches[75–78] were previously developed on metallic systems that may assist in the pursue of the modelling of conduction electrons on doped-2D magnets. If the electrical conductivity of CrX_3 (X=I, Br) is enhanced due to different chemical or physical processes, the values of the domain wall speeds shown in Figure 3 would be robust against such variations. Since the magnitude of

the Gilbert damping λ_G utilised in the simulations ($\lambda_G = 0.10$) is high than that expected for CrI_3 and $CrBr_3$[37], we intrinsically take into account additional dissipation effects in our simulations. Furthermore, investigations to clarify the effect of different dopants, concentration and their implications on both damping and the magnetic properties of 2D magnets are promptly needed. The emission of spin waves in the THz regime and the spin hydrodynamic behaviour observed for both halides, also merit further exploration on novel information technologies. On one hand, the design of sources, detectors and prototypes functioning in the THz-gap ($0.3-30$ THz)[79] provides the groundwork for the developments of high-end electronics on the low-end of the electromagnetic spectrum. The ultrathin character of 2D magnets, their flexibility in generating tunable frequencies, and inexpensive sample cost relative to expensive bulky compounds[79], make vdW layered materials a playground for applications. On the other hand, the use of magnons for information carrier at the μm-scale puts vdW sheets in the roadmap of post-semiconductor spin-wave technologies. The characteristic soliton features observed on the shock-waves in both ferromagnets and consequent low dissipation indicate that magnon-based data operations may be explored for information processing. In this sense, the development of an energy-efficient spin-wave transducer through vdW materials is one of the key steps for the ultimate goal of hybrid spin-wave computing systems.

Supplementary Materials

Methods, Supplementary Figures S1−S4, and Supplementary movies S1−S12.

Data Availability

The data that support the findings of this study are available within the paper and its Supplementary Information.

Competing interests

The Authors declare no conflict of interests.

Acknowledgments

RFLE acknowledges computational resources from the VIKING cluster provided by the University of York. EJGS acknowledges computational resources through CIRRUS Tier-2 HPC Service (ec131 Cirrus Project) CIRRUS@EPCC (http://www.cirrus.ac.uk) funded by the University of Edinburgh and EPSRC (EP/P020267/1); ARCHER UK National Supercomputing Service (http://www.archer.ac.uk) via Project d429. EJGS acknowledges the EPSRC Early Career Fellowship (EP/T021578/1) and the University of Edinburgh for funding support.

References

1. Beach, G. S. D., Tsoi, M. & Erskine, J. L. Current-induced domain wall motion. *Journal of Magnetism and Magnetic Materials* **320**, 1272–1281 (2008). URL http://www.sciencedirect.com/science/article/pii/S0304885307010141.

2. Tatara, G., Kohno, H. & Shibata, J. Microscopic approach to current-driven domain wall dynamics. *Physics Reports* **468**, 213 – 301 (2008). URL http://www.sciencedirect.com/science/article/pii/S0370157308002597.

3. Ralph, D. & Stiles, M. Spin transfer torques. *Journal of Magnetism and Magnetic Materials* **320**, 1190 – 1216 (2008). URL http://www.sciencedirect.com/science/article/pii/S0304885307010116.

4. Parkin, S. S. P., Hayashi, M. & Thomas, L. Magnetic domain-wall racetrack memory. *Science* **320**, 190–194 (2008). URL https://science.sciencemag.org/content/320/5873/190. https://science.sciencemag.org/content/320/5873/190.full.pdf.

5. Huang, B. *et al.* Layer-dependent ferromagnetism in a van der waals crystal down to the monolayer limit. *Nature* **546**, 270 EP – (2017). URL https://doi.org/10.1038/nature22391.

6. Gong, C. *et al.* Discovery of intrinsic ferromagnetism in two-dimensional van der waals crystals. *Nature* **546**, 265–269 (2017). URL http://dx.doi.org/10.1038/nature22060. Letter.

7. Guguchia, Z. *et al.* Magnetism in semiconducting molybdenum dichalcogenides. *Science Advances* **4** (2018). URL https://advances.sciencemag.org/content/4/12/eaat3672. https://advances.sciencemag.org/content/4/12/eaat3672.full.pdf.

8. Klein, D. R. *et al.* Probing magnetism in 2d van der waals crystalline insulators via electron tunneling. *Science* **360**, 1218–1222 (2018). URL http://science.sciencemag.org/content/360/6394/1218. http://science.sciencemag.org/content/360/6394/1218.full.pdf.

9. Allwood, D. A. *et al.* Magnetic domain-wall logic. *Science* **309**, 1688–1692 (2005). URL https://science.sciencemag.org/content/309/5741/1688. https://science.sciencemag.org/content/309/5741/1688.full.pdf.

10. Luo, Z. *et al.* Current-driven magnetic domain-wall logic. *Nature* **579**, 214–218 (2020). URL https://doi.org/10.1038/s41586-020-2061-y.

11. Xu, P. *et al.* An all-metallic logic gate based on current-driven domain wall motion. *Nature Nanotechnology* **3**, 97–100 (2008). URL https://doi.org/10.1038/nnano.2008.1.

12. Yang, S.-H., Ryu, K.-S. & Parkin, S. Domain-wall velocities of up to 750 m s-1 driven by exchange-coupling torque in synthetic antiferromagnets. *Nature Nanotechnology* **10**, 221–226 (2015). URL https://doi.org/10.1038/nnano.2014.324.

13. Woo, S. *et al.* Observation of room-temperature magnetic skyrmions and their current-driven dynamics in ultrathin metallic ferromagnets. *Nature Materials* **15**, 501–506 (2016). URL https://doi.org/10.1038/nmat4593.

14. Vélez, S. *et al.* High-speed domain wall racetracks in a magnetic insulator. *Nature Communications* **10**, 4750 (2019). URL https://doi.org/10.1038/s41467-019-12676-7.

15. Siddiqui, S. A., Han, J., Finley, J. T., Ross, C. A. & Liu, L. Current-induced domain wall motion in a compensated ferrimagnet. *Phys. Rev. Lett.* **121**, 057701 (2018). URL https://link.aps.org/doi/10.1103/PhysRevLett.121.057701.

16. Ryu, K.-S., Thomas, L., Yang, S.-H. & Parkin, S. Chiral spin torque at magnetic domain walls. *Nature Nanotechnology* **8**, 527–533 (2013). URL https://doi.org/10.1038/nnano.2013.102.

17. Rabinovich, M. & Trubetskov, D. *Oscillations and Waves: in Linear and Nonlinear Systems*. Mathematics and its Applications (Springer Netherlands, 2011). URL https://books.google.es/books?id=cUYfswEACAAJ.

18. Parkin, S. & Yang, S.-H. Memory on the racetrack. *Nature Nanotechnology* **10**, 195–198 (2015). URL https://doi.org/10.1038/nnano.2015.41.

19. Baltz, V. *et al.* Antiferromagnetic spintronics. *Rev. Mod. Phys.* **90**, 015005 (2018). URL https://link.aps.org/doi/10.1103/RevModPhys.90.015005.

20. Cowburn, R. P. & Welland, M. E. Room temperature magnetic quantum cellular automata. *Science* **287**, 1466–1468 (2000). URL https://science.sciencemag.org/content/287/5457/1466. https://science.sciencemag.org/content/287/5457/1466.full.pdf.

21. Allwood, D. A. *et al.* Submicrometer ferromagnetic not gate and shift register. *Science* **296**, 2003–2006 (2002). URL https://science.sciencemag.org/content/296/5575/2003. https://science.sciencemag.org/content/296/5575/2003.full.pdf.

22. Diegel, M., Glathe, S., Mattheis, R., Scherzinger, M. & Halder, E. A new four bit magnetic domain wall based multiturn counter. *IEEE Transactions on Magnetics* **45**, 3792–3795 (2009).

23. Kim, H. H. *et al.* One million percent tunnel magnetoresistance in a magnetic van der waals heterostructure. *Nano Letters* **18**, 4885–4890 (2018). URL https://doi.org/10.1021/acs.nanolett.8b01552.

24. Ghazaryan, D. *et al.* Magnon-assisted tunnelling in van der waals heterostructures based on crbr3. *Nature Electronics* **1**, 344–349 (2018). URL https://doi.org/10.1038/s41928-018-0087-z.

25. Cantos-Prieto, F. *et al.* Layer-dependent mechanical properties and enhanced plasticity in the van der waals chromium trihalide magnets. *Nano Letters* **21**, 3379–3385 (2021). URL https://doi.org/10.1021/acs.nanolett.0c04794.

26. Chappert, C., Fert, A. & Van Dau, F. N. The emergence of spin electronics in data storage. *Nature Materials* **6**, 813–823 (2007). URL https://doi.org/10.1038/nmat2024.

27. Manchon, A. *et al.* Current-induced spin-orbit torques in ferromagnetic and antiferromagnetic systems. *Rev. Mod. Phys.* **91**, 035004 (2019). URL https://link.aps.org/doi/10.1103/RevModPhys.91.035004.

449 28. Gupta, V. *et al.* Manipulation of the van der waals magnet cr2ge2te6 by spin–orbit torques.
450 *Nano Letters* **20**, 7482–7488 (2020). URL https://doi.org/10.1021/acs.nanolett.
451 0c02965.

452 29. Wang, X. *et al.* Current-driven magnetization switching in a van der waals ferromag-
453 net fe3gete2. *Science Advances* **5** (2019). URL https://advances.sciencemag.
454 org/content/5/8/eaaw8904. https://advances.sciencemag.org/content/5/8/
455 eaaw8904.full.pdf.

456 30. Wahab, D. A. *et al.* Quantum rescaling, domain metastability, and hybrid domain-
457 walls in 2d cri3 magnets. *Advanced Materials* **33**, 2004138 (2021). URL
458 https://onlinelibrary.wiley.com/doi/abs/10.1002/adma.202004138. https://
459 onlinelibrary.wiley.com/doi/pdf/10.1002/adma.202004138.

460 31. Sun, Q.-C. *et al.* Magnetic domains and domain wall pinning in atomically thin crbr3 revealed
461 by nanoscale imaging. *Nature Communications* **12**, 1989 (2021). URL https://doi.org/
462 10.1038/s41467-021-22239-4.

463 32. Kartsev, A., Augustin, M., Evans, R. F. L., Novoselov, K. S. & Santos, E. J. G. Biquadratic ex-
464 change interactions in two-dimensional magnets. *npj Computational Materials* **6**, 150 (2020).
465 URL https://doi.org/10.1038/s41524-020-00416-1.

466 33. Soriano, D., Katsnelson, M. I. & Fernández-Rossier, J. Magnetic two-dimensional chromium
467 trihalides: A theoretical perspective. *Nano Letters* **20**, 6225–6234 (2020). URL https:
468 //doi.org/10.1021/acs.nanolett.0c02381.

34. Chen, L. *et al.* Topological spin excitations in honeycomb ferromagnet cri_3. *Phys. Rev. X* **8**, 041028 (2018). URL https://link.aps.org/doi/10.1103/PhysRevX.8.041028.

35. Wildes, A. R., Zhitomirsky, M. E., Ziman, T., Lançon, D. & Walker, H. C. Evidence for biquadratic exchange in the quasi-two-dimensional antiferromagnet feps3. *Journal of Applied Physics* **127**, 223903 (2020). URL https://doi.org/10.1063/5.0009114. https://doi.org/10.1063/5.0009114.

36. Augustin, M., Jenkins, S., Evans, R. F. L., Novoselov, K. S. & Santos, E. J. G. Properties and dynamics of meron topological spin textures in the two-dimensional magnet crcl3. *Nature Communications* **12**, 185 (2021). URL https://doi.org/10.1038/s41467-020-20497-2.

37. Kapoor, L. N. *et al.* Observation of standing spin waves in a van der waals magnetic material. *Advanced Materials* **33**, 2005105 (2021). URL https://onlinelibrary.wiley.com/doi/abs/10.1002/adma.202005105. https://onlinelibrary.wiley.com/doi/pdf/10.1002/adma.202005105.

38. Abramchuk, M. *et al.* Controlling magnetic and optical properties of the van der waals crystal crcl3xbrx via mixed halide chemistry. *Advanced Materials* **30**, 1801325 (2018). URL https://onlinelibrary.wiley.com/doi/abs/10.1002/adma.201801325. https://onlinelibrary.wiley.com/doi/pdf/10.1002/adma.201801325.

39. Jiang, S., Li, L., Wang, Z., Mak, K. F. & Shan, J. Controlling magnetism in 2d cri3 by electrostatic doping. *Nature Nanotechnology* **13**, 549–553 (2018). URL https://doi.org/

10.1038/s41565-018-0135-x.

40. Kim, H. H. *et al.* Evolution of interlayer and intralayer magnetism in three atomically thin chromium trihalides. *PNAS* **116**, 11131–11136 (2019).

41. Hubert, A. & Schafer, R. *Magnetic Domains: The Analysis of Magnetic Microstructures* (Springer Science and Business Media, 2008).

42. Schryer, N. L. & Walker, L. R. The motion of 180° domain walls in uniform dc magnetic fields. *Journal of Applied Physics* **45**, 5406–5421 (1974). URL https://doi.org/10.1063/1.1663252. https://doi.org/10.1063/1.1663252.

43. Metaxas, P. J. *et al.* Creep and flow regimes of magnetic domain-wall motion in ultrathin Pt/Co/Pt films with perpendicular anisotropy. *Phys. Rev. Lett.* **99**, 217208 (2007). URL https://link.aps.org/doi/10.1103/PhysRevLett.99.217208.

44. Pizzini, S. *et al.* Chirality-induced asymmetric magnetic nucleation in Pt/Co/alo$_x$ ultrathin microstructures. *Phys. Rev. Lett.* **113**, 047203 (2014). URL https://link.aps.org/doi/10.1103/PhysRevLett.113.047203.

45. Bode, M. Spin-polarized scanning tunnelling microscopy. *Reports on Progress in Physics* **66**, 523–582 (2003). URL https://doi.org/10.1088%2F0034-4885%2F66%2F4%2F203.

46. Casola, F., van der Sar, T. & Yacoby, A. Probing condensed matter physics with magnetometry based on nitrogen-vacancy centres in diamond. *Nature Reviews Materials* **3**, 17088 (2018). URL https://doi.org/10.1038/natrevmats.2017.88.

508 47. Yamanouchi, M., Chiba, D., Matsukura, F., Dietl, T. & Ohno, H. Velocity of domain-wall
509 motion induced by electrical current in the ferromagnetic semiconductor (ga,mn)as. *Phys.*
510 *Rev. Lett.* **96**, 096601 (2006). URL https://link.aps.org/doi/10.1103/PhysRevLett.
511 96.096601.

512 48. Miron, I. M. *et al.* Fast current-induced domain-wall motion controlled by the rashba effect.
513 *Nature Materials* **10**, 419–423 (2011). URL https://doi.org/10.1038/nmat3020.

514 49. Emori, S., Bauer, U., Ahn, S.-M., Martinez, E. & Beach, G. S. D. Current-driven dynamics
515 of chiral ferromagnetic domain walls. *Nature Materials* **12**, 611–616 (2013). URL https:
516 //doi.org/10.1038/nmat3675.

517 50. Wieser, R., Vedmedenko, E. Y. & Wiesendanger, R. Domain wall motion damped by the
518 emission of spin waves. *Phys. Rev. B* **81**, 024405 (2010). URL https://link.aps.org/
519 doi/10.1103/PhysRevB.81.024405.

520 51. Zhang, S. & Li, Z. Roles of nonequilibrium conduction electrons on the magnetization dy-
521 namics of ferromagnets. *Phys. Rev. Lett.* **93**, 127204 (2004). URL https://link.aps.org/
522 doi/10.1103/PhysRevLett.93.127204.

523 52. Thiaville, A., Nakatani, Y., Miltat, J. & Suzuki, Y. Micromagnetic understanding of current-
524 driven domain wall motion in patterned nanowires. *Europhys. Lett.* **69**, 990–996 (2005). URL
525 https://doi.org/10.1209/epl/i2004-10452-6.

526 53. Hayashi, M. *et al.* Influence of current on field-driven domain wall motion in permalloy
527 nanowires from time resolved measurements of anisotropic magnetoresistance. *Phys. Rev.*

Lett. **96**, 197207 (2006). URL https://link.aps.org/doi/10.1103/PhysRevLett.96.197207.

54. Wang, X. S. & Wang, X. R. Spin wave emission in field-driven domain wall motion. *Phys. Rev. B* **90**, 184415 (2014). URL https://link.aps.org/doi/10.1103/PhysRevB.90.184415.

55. Lederer, P. & Mills, D. L. Possible experimental test of the band theory of magnetism. *Phys. Rev.* **148**, 542–547 (1966). URL https://link.aps.org/doi/10.1103/PhysRev.148.542.

56. Vlaminck, V. & Bailleul, M. Current-induced spin-wave doppler shift. *Science* **322**, 410–413 (2008). URL https://science.sciencemag.org/content/322/5900/410. https://science.sciencemag.org/content/322/5900/410.full.pdf.

57. Zhu, M., Dennis, C. L. & McMichael, R. D. Temperature dependence of magnetization drift velocity and current polarization in $ni_{80}fe_{20}$ by spin-wave doppler measurements. *Phys. Rev. B* **81**, 140407 (2010). URL https://link.aps.org/doi/10.1103/PhysRevB.81.140407.

58. Sekiguchi, K. *et al.* Time-domain measurement of current-induced spin wave dynamics. *Phys. Rev. Lett.* **108**, 017203 (2012). URL https://link.aps.org/doi/10.1103/PhysRevLett.108.017203.

59. Whitham, G. B. *Linear and nonlinear waves* (John Wiley & Sons Inc, 1974).

60. Bonnefoy, F. *et al.* From modulational instability to focusing dam breaks in water waves. *Phys. Rev. Fluids* **5**, 034802 (2020).

547 61. Marcucci, G. *et al.* Topological control of extreme waves. *Nature Communications* **10**, 5090
548 (2019).

549 62. Kevrekidis, P. G., Frantzeskakis, D. J. & Carretero-González, R. *The Defocusing Nonlinear*
550 *Schrödinger Equation* (SIAM, Philadelphia, 2015).

551 63. Mohseni, S. M. *et al.* Spin torque generated magnetic droplet solitons. *Science* **339**, 1295–
552 1298 (2013).

553 64. Iacocca, E. *et al.* Spin-current-mediated rapid magnon localization and coalescence after ul-
554 trafast optical pumping of ferrimagnetic alloys. *Nature Communications* **10**, 1756 (2019).

555 65. Iacocca, E., Silva, T. J. & Hoefer, M. A. Breaking of galilean invariance in the hydrodynamic
556 formulation of ferromagnetic thin films. *Phys. Rev. Lett.* **118**, 017203 (2017).

557 66. Ivanov, S. K., Kamchatnov, A. M., Congy, T. & Pavloff, N. Solution of the riemann problem
558 for polarization waves in a two-component bose-einstein condensate. *Phys. Rev. E* **96**, 062202
559 (2017).

560 67. Gelash, A. *et al.* Bound state soliton gas dynamics underlying the spontaneous modulational
561 instability. *Phys. Rev. Lett.* **123**, 234102 (2019).

562 68. Cornelissen, L. J., Liu, J., Duine, R. A., Youssef, J. B. & van Wees, B. J. Long-distance
563 transport of magnon spin information in a magnetic insulator at room temperature. *Nature*
564 *Physics* **11**, 1022–1026 (2015). URL `https://doi.org/10.1038/nphys3465`.

69. Liu, C. *et al.* Long-distance propagation of short-wavelength spin waves. *Nature Communications* **9**, 738 (2018). URL https://doi.org/10.1038/s41467-018-03199-8.

70. Kajiwara, Y. *et al.* Transmission of electrical signals by spin-wave interconversion in a magnetic insulator. *Nature* **464**, 262–266 (2010). URL https://doi.org/10.1038/nature08876.

71. Xing, W. *et al.* Magnon transport in quasi-two-dimensional van der waals antiferromagnets. *Phys. Rev. X* **9**, 011026 (2019). URL https://link.aps.org/doi/10.1103/PhysRevX.9.011026.

72. Bedoya-Pinto, A. *et al.* Intrinsic 2d-xy ferromagnetism in a van der waals monolayer. *arXiv:2006.07605* .

73. Kezilebieke, S. *et al.* Electronic and magnetic characterization of epitaxial crbr3 monolayers on a superconducting substrate. *Advanced Materials* **33**, 2006850 (2021). URL https://onlinelibrary.wiley.com/doi/abs/10.1002/adma.202006850. https://onlinelibrary.wiley.com/doi/pdf/10.1002/adma.202006850.

74. Wang, H., Fan, F., Zhu, S. & Wu, H. Doping enhanced ferromagnetism and induced half-metallicity in CrI 3 monolayer. *EPL (Europhysics Letters)* **114**, 47001 (2016). URL https://doi.org/10.1209/0295-5075/114/47001.

75. Zhang, S. & Zhang, S. S.-L. Generalization of the landau-lifshitz-gilbert equation for conducting ferromagnets. *Phys. Rev. Lett.* **102**, 086601 (2009). URL https://link.aps.org/doi/10.1103/PhysRevLett.102.086601.

585 76. Kim, K.-W., Moon, J.-H., Lee, K.-J. & Lee, H.-W. Prediction of giant spin motive force due to
586 rashba spin-orbit coupling. *Phys. Rev. Lett.* **108**, 217202 (2012). URL https://link.aps.
587 org/doi/10.1103/PhysRevLett.108.217202.

588 77. Petrović, M. D., Bajpai, U., Plecháč, P. & Nikolić, B. K. Annihilation of topological solitons
589 in magnetism with spin-wave burst finale: Role of nonequilibrium electrons causing nonlocal
590 damping and spin pumping over ultrabroadband frequency range. *Phys. Rev. B* **104**, L020407
591 (2021). URL https://link.aps.org/doi/10.1103/PhysRevB.104.L020407.

592 78. Weindler, T. *et al.* Magnetic damping: Domain wall dynamics versus local ferromagnetic
593 resonance. *Phys. Rev. Lett.* **113**, 237204 (2014). URL https://link.aps.org/doi/10.
594 1103/PhysRevLett.113.237204.

595 79. Dhillon, S. S. *et al.* The 2017 terahertz science and technology roadmap. *Journal of Physics*
596 *D: Applied Physics* **50**, 043001 (2017). URL https://doi.org/10.1088/1361-6463/50/
597 4/043001.

Figure captions

Figure 1: **Magnetic domains at different temperatures and fields. a-e,** Dynamical spin configurations of monolayer $CrBr_3$ during zero-field cooling (0 mT) at different temperatures. The out-of-plane magnetization M_z (a.u.) is used to follow the evolution of the magnetic domains from 40 K down to 0 K. **f-j, k-o,** and **p-t,** Similar as **a-e,** but at magnetic fields of 5 mT, 11 mT and 50 mT, respectively. Temperatures at the top row correspond to all panels in the same column. Time scale spanned up to 2.5 ns till 0 K is achieved. Further evolution are observed at later times as shown in Supplementary Movies S1-S4.

Figure 2: **Hybrid domain walls with Néel-Bloch characteristics. a-b,** Global and local views, respectively, of a snapshot for one of the spin configurations projected along M_z (colour map) showing the formation of a domain wall in monolayer $CrBr_3$. The total strip in **a** is 400×50 nm. Only Cr atoms are showed in the honeycomb lattice arrangement of monolayer $CrBr_3$. The system is at 0 K without any external fields or currents. **c-d,** Side and top views, respectively, of the rotation of the magnetization along the domain wall. Both M_x and M_y show variations along the wall altogether with M_z which indicate a hybrid character of the domain wall with Néel and Bloch features. Colours follow the scale bar in **a**. The small area around the domain wall highlighted in **a** corresponds to **c**. **e-f,** Variation of the magnetization along the domain wall projected along the in-plane components (M_x, M_y) and M_z, respectively. Fitting lines are obtained using Eqs.2-3.

Figure 3: **Current- and field-induced domain wall dynamics in 2D ferromagnets. a,** Initial domain wall configuration for monolayer $CrBr_3$ at no external driving forces (j=0, B=0). The domain wall is initially equilibrated for up to 4 ns to ensure convergence of the spin orientations along the wall and width. The same final configuration is utilised for both field- and current-driven domain wall motion. Similar procedure is undertaken to monolayer CrI_3. **b-c,** Snapshots of the domain wall dynamics in $CrBr_3$ induced by magnetic fields (0.05 T, 1.50 T) and electric currents (8.7×10^9 A cm^{-2}, 4.3×10^9 A cm^{-2}), respectively. The edges used in the simulations are highlighted at B=1.50 T with dangling-bond and zig-zag at the top and bottom of the layer, respectively. Deformations observed near the domain wall at $j = 4.3 \times 10^9$ A cm^{-2} are highlighted by the dashed rectangle. **d,** Zoom-in of the local spin-configurations at $j = 4.3 \times 10^9$ A cm^{-2}) with colour scale showing the variations of the spin orientations along M_z induced by the large current density.

Figure 4: **Domain wall speeds and spin wave frequency. a-b,** Calculated domain wall velocities v versus the applied magnetic field B for $CrBr_3$ and CrI_3, respectively. The vertical solid lines indicate the region where the nucleation of magnetic bubbles starts in each material as those shown in **b** at 1.50 T for $CrBr_3$. A fit using $v = \mu(B - B_o)$, where μ is the domain wall mobility and B_o is the onset field, reproduces accurately the atomistic simulation data with linear regression coefficients $R^2 = 0.99$ and a root-mean-square-error of 0.0074. The field is applied perpendicular to the surface following the easy-axis of the materials. **c-d,** Variations of v as a function of the current density j for $CrBr_3$ and CrI_3, respectively. Two regimes are observed in the internal dynamics of the wall before and after the Walker breakdown (j_w) with the wall motion being in steady and precessional states, respectively. We could extract $j_w^{CrBr_3} = 4.8 \times 10^9$ A cm^{-2} and $j_w^{CrI_3} = 12.0 \times 10^9$ A cm^{-2}. Both steady and precessional regimes on the domain-wall dynamics can be modelled using a 1D model as described in the text. The insets show the velocities at lower values of current within $j \leq 8.5 \times 10^8$ A cm^{-2}. **e-f,** Frequencies ω_B(THz) and ω_J(THz) of the emitted spin-waves during the domain-wall motion as a function of B and j, respectively, for $CrBr_3$ and CrI_3. Dashed lines are corresponding fits to Eqs. 5−6. Similar data labelling applies for **e** and **f**.

Figure 5: **Modulational instability in 2D magnets. a-c,** Snapshots of the magnetisation along M_z and M_x magnetisation components at different times at 18 ps, 40 ps and 78 ps, respectively. **d,** Amplitude of M_x as a function of time at different current densities.

Figure 6: **Long range spin-wave propagation. a-c,** Snapshots of spin-dynamics at 20 ps, 200 ps and 600 ps, respectively, under a current density of 1.56×10^{10} A cm^{-2}. M_z is used to show the variations of the domain wall with the colour scale along the length of the ribbon. A separation of the motion of the original domain wall (soliton edge) and the shock waves can be observed between a wave train (modulationally unstable) propagating throughout the system. **d,** Colour-plot of the variations of M_z with the propagation time along a 2-μm ribbon of $CrBr_3$ at a current density of 1.56×10^{10} A cm^{-2}. The different line-cuts correspond to the several waveforms moving into the systems as shown in **e-g**. The dashed lines are given by $s^+ = 5773$ m s$^{-1} \pm 0.84$ m s^{-1}, $s_1^- = 1328$ m s$^{-1} \pm 1.7$ m s^{-1} and $s_2^- = 882$ m s$^{-1} \pm 1.8$ m s^{-1}. **e-f,** Spectral density (arb. units) extracted from the fast Fourier transform of the M_z component as function of time in **d** along velocities s^+ and s_2^-, respectively. The characteristic frequencies of the shock waves and the domain-wall wake can be identified as $\nu_{SW} = 177.5$ GHz± 1.25 GHz and $\nu_{wake} = 6.66 \pm 1.66$ GHz, respectively.

Figures

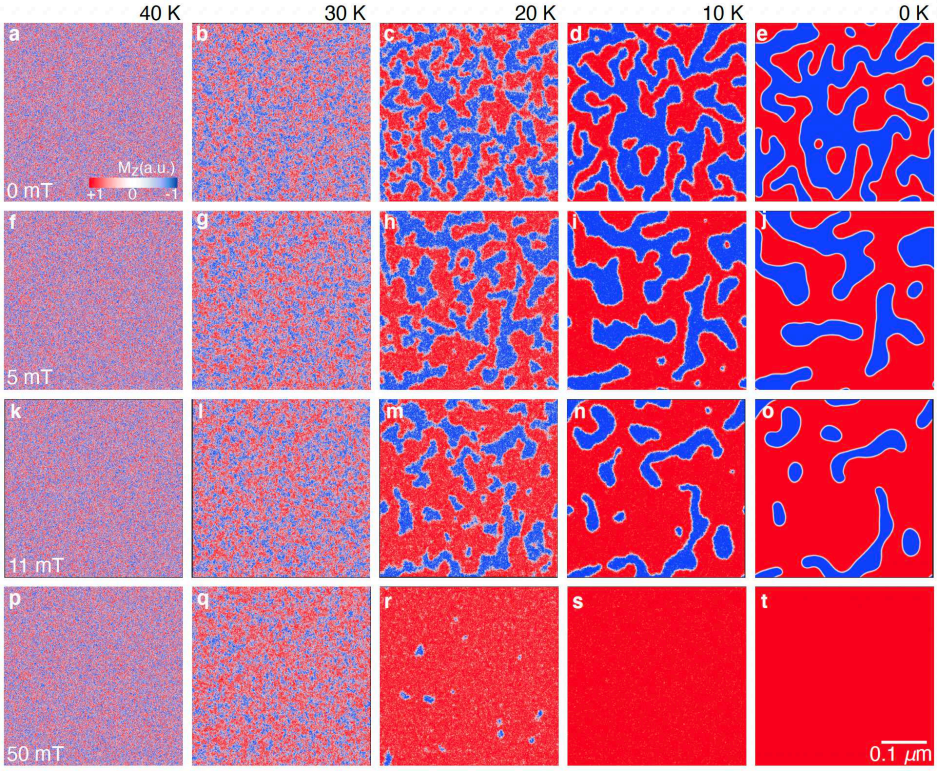

Figure 1

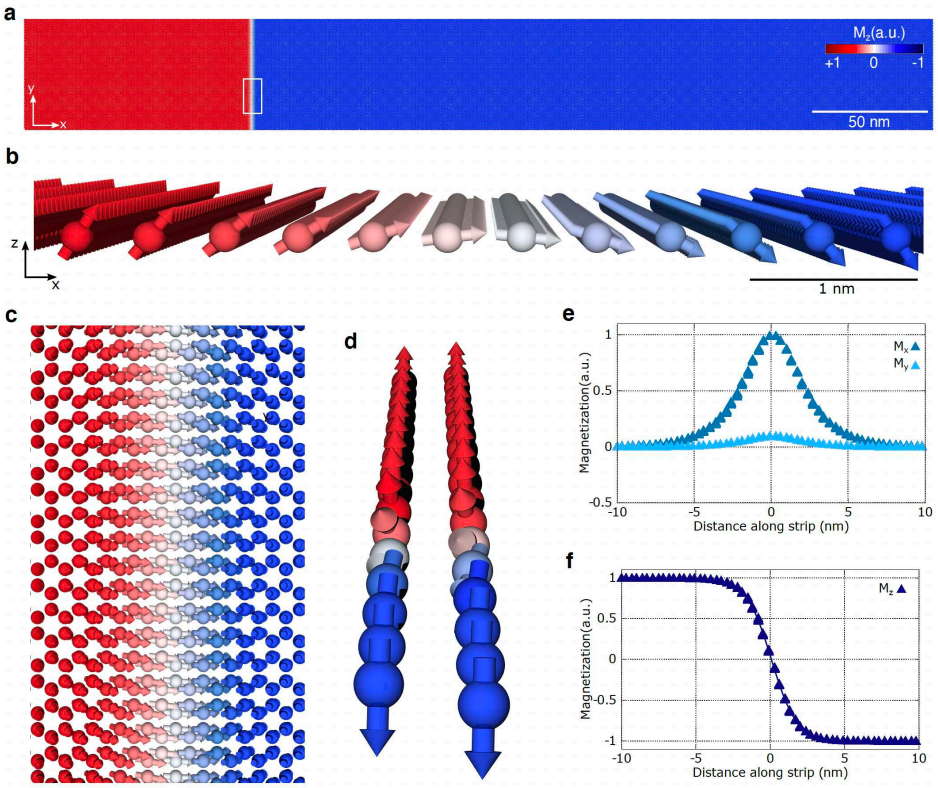

Figure 2

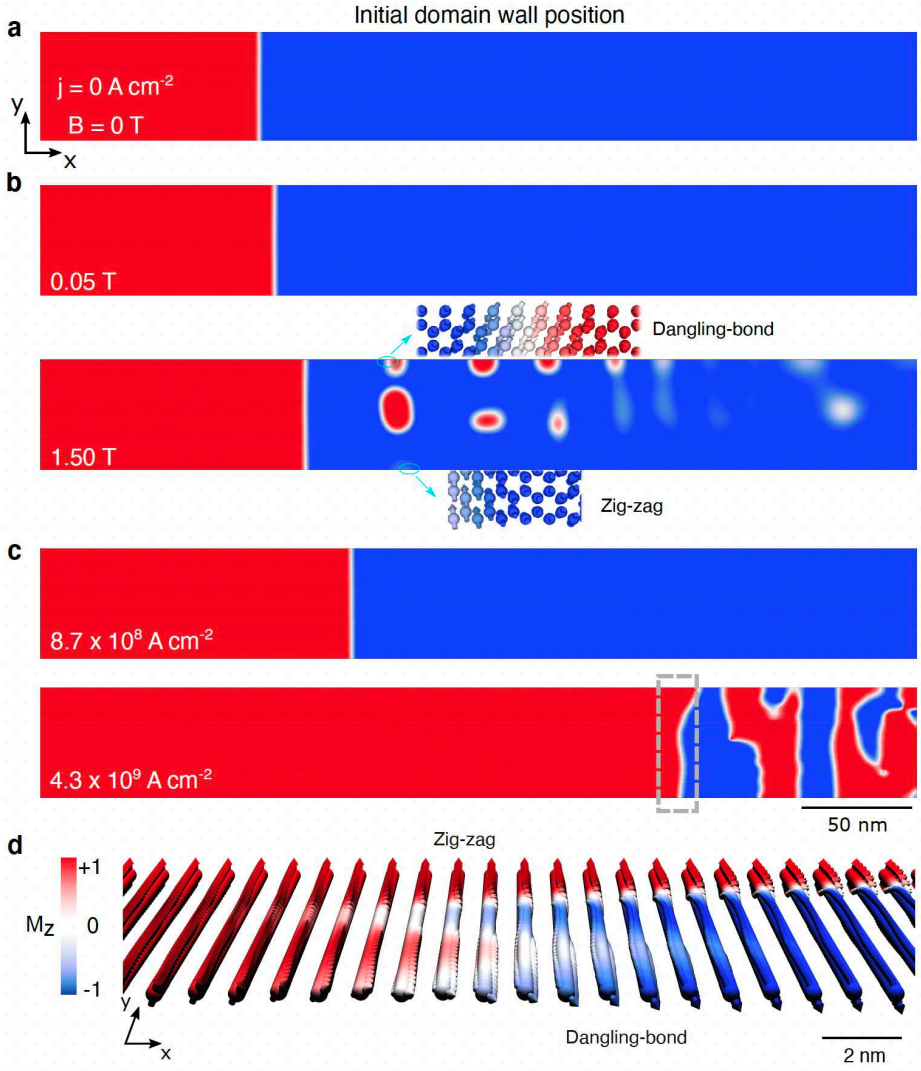

Figure 3

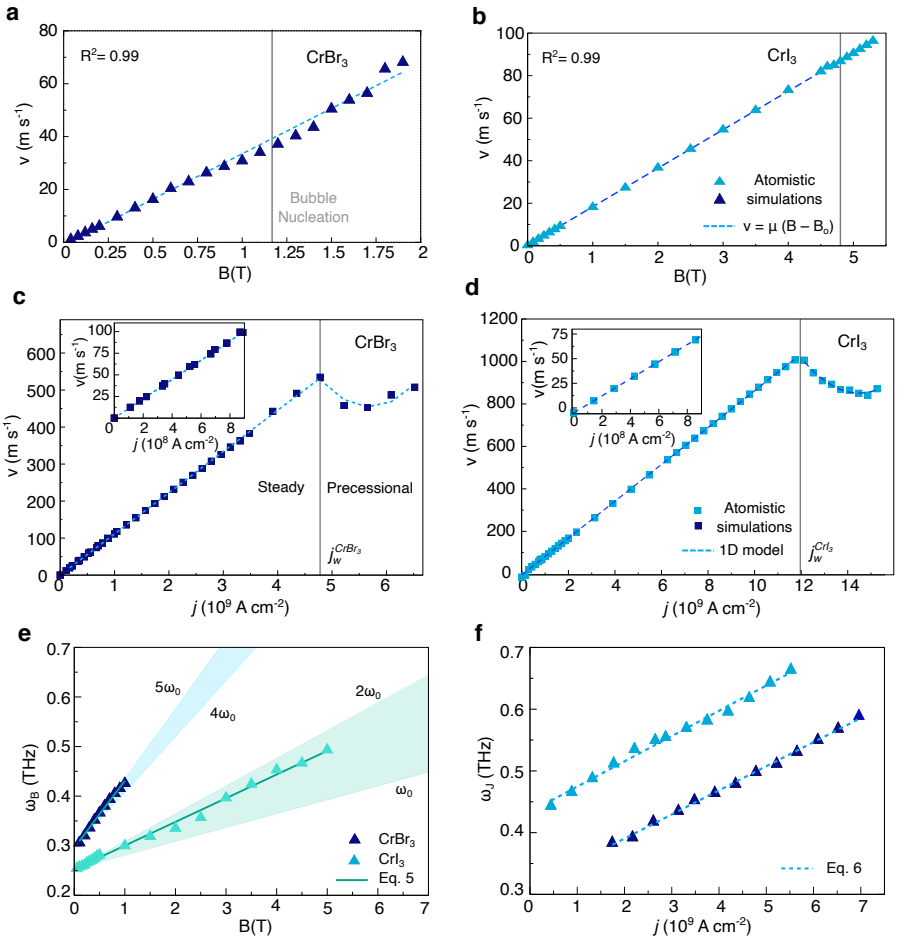

Figure 4

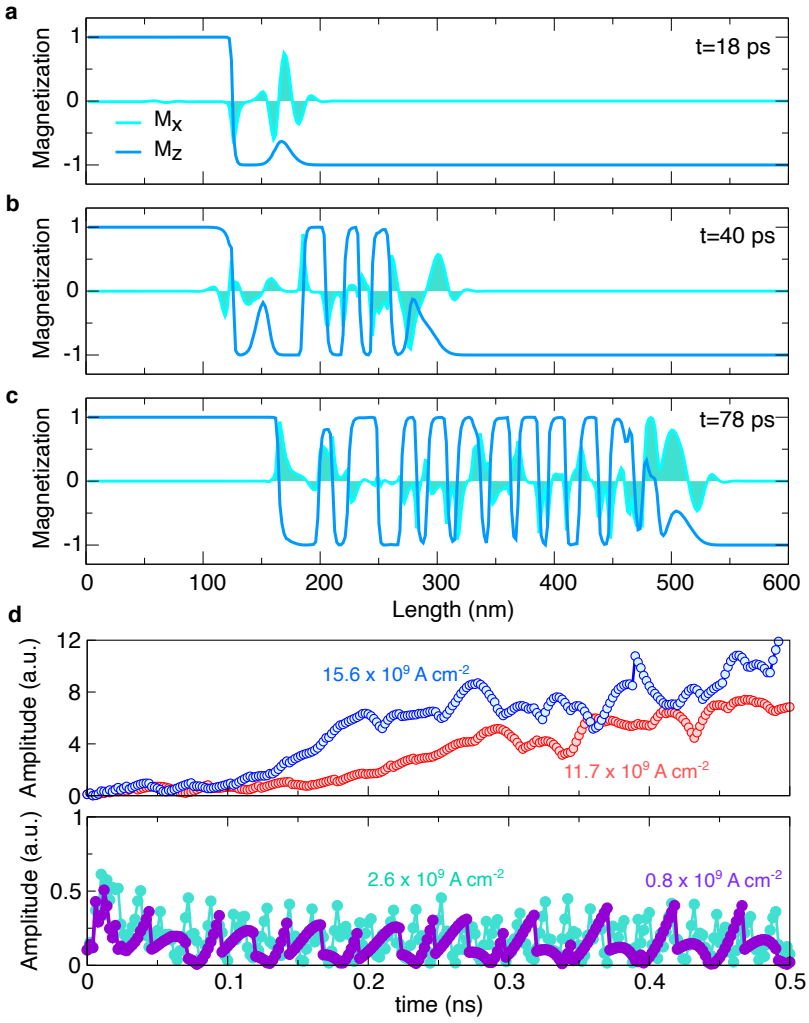

Figure 5

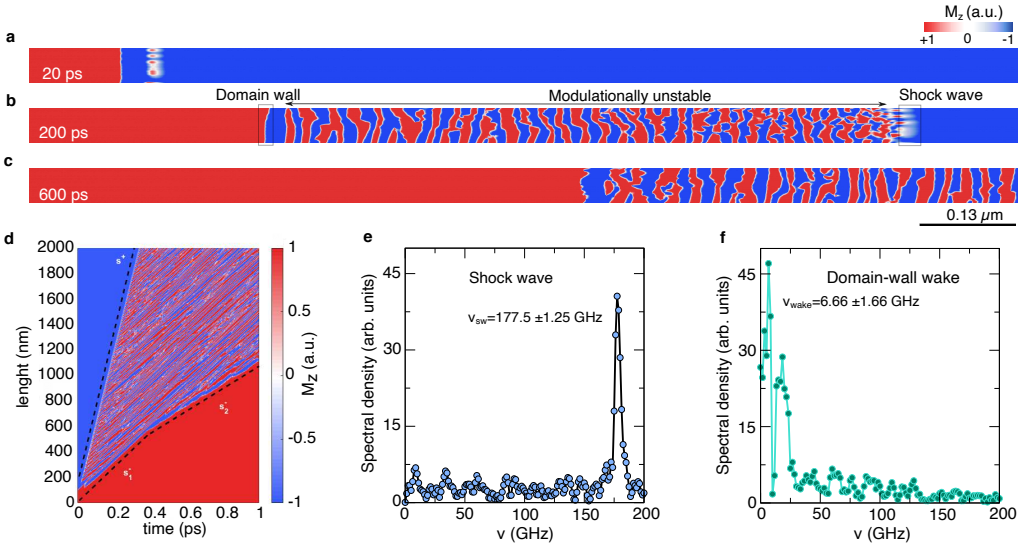

Figure 6